

Elastically driven surface plumes in rimming flow of a non-Newtonian fluid

Gabriel Seiden* and Victor Steinberg

Department of Physics of Complex Systems, The Weizmann Institute of Science, Rehovot 76100, Israel

(Received 22 June 2012; published 29 November 2012)

A polymer solution partially filling a rotating horizontal drum undergoes an elastically driven instability at low Reynolds numbers. This instability manifests itself through localized plumelike bursts, perturbing the free liquid surface. Here we present an expanded experimental account regarding the dynamics of individual plumes and the statistics pertaining to the complex collective interaction between plumes, which leads to plume coagulation. We also present a detailed description of an optical technique that enables the visualization and measurement of surface perturbations in coating flows within a rotating horizontal drum.

DOI: [10.1103/PhysRevE.86.056320](https://doi.org/10.1103/PhysRevE.86.056320)

PACS number(s): 47.32.-y, 89.75.Da, 89.75.Fb, 42.15.Eq

I. INTRODUCTION

The rotating horizontal drum is a unique experimental configuration that has served as a fertile tool in the investigation of phenomena as diverse as avalanches in granular material and solitary waves in pure liquids (see [1] and references therein). Recent years have seen intensified scientific activity focusing on the different realizations of rotating drum flows. This has led to a better understanding of underlying physical mechanisms, such as mixing of granular media. In addition to the importance of the rotating drum apparatus from a basic science perspective, it has numerous practical applications (e.g., mixing in the pharmaceutical industry).

Rimming flow is a particular realization of rotating drum flows, whereby a thin liquid layer exhibits different instabilities and dynamical states as the rotation rate Ω is varied between the quiescent pool limit and the centrifugal limit (see, e.g., [2–5]). These include solitary waves observed on the discontinuous liquid front at low Ω [2], a steady “shark teeth” pattern observed at moderate Ω [3], and periodically spaced vertical liquid walls (also termed “Hygrocyts” [5]) at higher values of the control parameter. Instabilities associated with the liquid front have mainly been investigated in the past through plain image acquisition. The strong refraction of light rays at the liquid front results in a dark line corresponding to the instantaneous location of the front. This enables a detailed analysis of the one-dimensional (1D) dynamics associated with the ridge. The intriguing dynamics associated with the free liquid surface was, however, left largely unexplored.

In a recently published article [6], we employed a specifically designed optical contrast technique in order to observe perturbations to the free surface *away* from the front for the case of a dilute polymer solution. Through the use of this technique, it was shown that the free surface is strongly perturbed by chaotic surface plumes which originate at the front and move upstream where they eventually decay. It was also shown that the dynamical evolution of these plumes is affected by plume coalescence or merging, resulting in a Kolmogorov-type power-law scaling cascade.

In the present work, we present an expanded experimental investigation into the dynamics of the elastically driven surface

plumes. This includes the evolution of individual plumes and the statistics resulting from the complex interaction between neighboring plumes. Emphasis is also placed on the optical contrast technique (OCT) used to visualize and quantitatively measure surface perturbations in rimming flows.

The article is arranged as follows. In Sec. II, we present a detailed description of the experimental setup. In particular, we elaborate on the underlying principle of OCT (Sec. II B) and we present a rigorous derivation of angular surface perturbations from intensity images of the free liquid surface (Sec. II C). Then, in Sec. III A, we present experimental results on the dynamics of a single surface plume, followed by an investigation of merging plumes. We then present results on the statistics pertaining to the collective interaction of surface plumes and in particular the time-independent area cascade (Sec. III C). In Sec. IV, we conclude with a discussion.

II. EXPERIMENTAL APPARATUS**A. The rotating horizontal drum**

A schematic of the rotating drum configuration used in the study of rimming flow phenomena is depicted in Fig. 1. The main part of the setup is a mechanical device designed to rotate transparent tubes of radius R about a horizontal axis at a constant rate Ω via a dc motor (the actual frame holding the tube and the motor are not shown in the illustration). Two cameras, one at right angles to the rotation axis and at an angle γ to the vertical plane through the axis (CCD), and the other positioned *on axis* facing a transparent side wall (reflex camera), are used to observe the liquid layer. The CCD camera is used to record the dynamics on the free surface while the reflex camera is used in order to obtain the profile of the liquid front at each rotation rate. The latter information is used to obtain a quantitative measurement of the perturbed free surface (see Sec. II C).

The cylinder used in our experiment had an inner radius $R = 1.83$ cm and a length $l = 22.3$ cm. The cylinder was partially filled with a dilute solution of polyacrylamide (PAAm) in a viscous sugar solution. Three control parameters were varied in our experiments: the rotation rate (Ω), the polymer concentration (c_p), and the volume fraction (V^*). The rotation rate range explored in the experiments was $0.02 \lesssim \Omega \lesssim 0.3$ s⁻¹. The polymer concentrations used in our experiments were $c_p = 20, 40, 80,$ and 100 ppm. The molecular

*gabriel.seiden@weizmann.ac.il

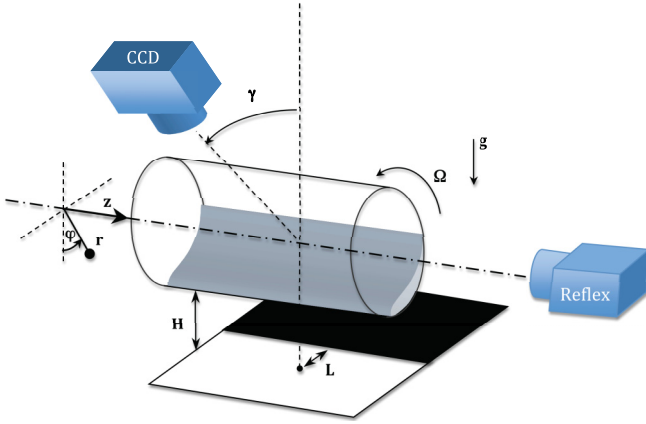


FIG. 1. (Color online) Illustration of a rotating drum setup used in the investigation of surface perturbations. A horizontal drum with an inner radius R rotates at a constant rate Ω about its axis. Two cameras are used to record information regarding the dynamics of the liquid layer. A CCD camera is positioned at right angles to the axis of rotation and at an angle γ to the vertical plane. A reflex camera is positioned on axis, facing a transparent end wall. A split black-and-white plane is placed underneath the drum. The distance between the black-and-white interface and the vertical plane through the axis of rotation is L .

weight of the polymer was $M_w = 18$ MDa (Polysciences Inc.) and the viscosity of the sugar syrup was $\eta = 114$ cP. The corresponding polymer relaxation time was $\lambda \cong 11$ s.¹ The reader is referred to [7] for more details regarding the preparation and rheological properties of the polymer solution. The volume fractions used in our experiments were $V^* = 0.1$ and 0.25 .

B. Underlying principle of OCT

Perturbations to the free surface in the vicinity of the liquid front are visualized through the use of OCT. This technique makes use of the fact that at the locations of surface perturbations, transmitted light rays are refracted differently relative to the rays refracting at the unperturbed surrounding. Figure 2 schematically depicts the underlying principle of OCT. A split black-and-white plane is located below the rotating cylinder and is homogeneously illuminated with a white light source. In what follows, we shall use a cylindrical coordinate system (r, φ, z) with its z axis coinciding with the rotation axis (see Fig. 1). We shall denote the distance between the black-and-white plane and the outer wall of the cylinder by H and the distance between the black-and-white interface and the vertical plane through the axis of rotation by L .

In the steady-state scenario, depicted in Fig. 2(a), where the recirculating flow within the pool is two-dimensional, light rays emerging from the white part of the contrast plane [CP in Fig. 2(a)] pass through the cylinder wall and liquid onto the CCD camera. While these rays are somewhat deflected in the r - φ plane due to the nonplanar interfaces of the cylinder and

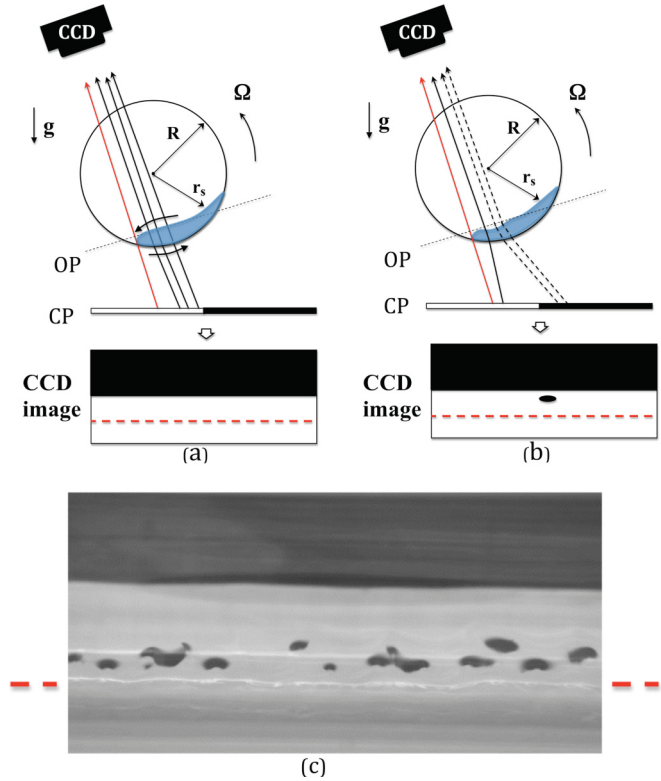


FIG. 2. (Color online) Optical contrast method for detecting surface plumes. (a) On-axis view of the stationary flow experienced by a viscous fluid partially filling a rotating horizontal drum. OP is the object plane of the CCD, and CP is the black-and-white contrast plane. Rays emerging from the illuminated white part of CP pass through the liquid onto the CCD. (b) Same as in (a), but with a perturbation to the surface. Black dashed lines represent the passage of rays which originated from the white part for the undisturbed case. A dark spot is seen in the CCD image as a result of the absence of these rays. (c) An example of a CCD image recording surface plumes using contrast plane technique. The red dashed line represents the undisturbed front line. Reproduced with permission from [6].

free liquid surface, the image captured by the CCD is that of a split black-and-white rectangle [lower part of Fig. 2(a)]. If, however, the liquid surface is perturbed, a bundle of light rays, which in the steady state case emerged from the white part of the CP, is now absent due to the strong refraction at the local surface perturbation. As a result, a dark spot can be observed at the corresponding location in the CCD image [Fig. 2(b)]. Figure 2(c) shows a typical image of surface perturbations observed through the use of OCT.

Setting the CCD angle γ and the position of the black-and-white interface through H and L is done prior to an experimental run. These values depend on the angular location of the liquid front φ_f . An estimate of the latter, for a liquid of density ρ and viscosity η , is given through comparing viscous and gravity forces acting on the liquid layer:

$$\varphi_f \approx \sin^{-1} \left(\frac{4\eta\Omega}{g\rho V^{*2}R} \frac{\Phi_0}{2\pi} \right) - \frac{1}{2}\Phi_0, \quad (1)$$

where the central angle Φ_0 pertaining to the liquid pool segment at rest ($\Omega = 0$) is given through the relationship $\Phi_0 - \sin(\Phi_0) = 2\pi V^*$ (V^* being the fluid volume fraction).

¹In one exception, described in Sec. III B, we used a polymer solution with a lower relaxation time. This was achieved through preparing the polymer solution with a lower amount of NaCl additive.

In general, one seeks to view a large enough area beyond the front, so that the whole field of activity on the free surface will be recorded. However, choosing a large value of L (for fixed γ and H) will inevitably result in a loss of resolution with respect to surface perturbations. This is due to the finite amount of deflection of rays passing through surface perturbations, relative to the unperturbed steady scenario.

For given values of φ_f , γ , H and the front angle α_f (i.e., corresponding to the tangential to the liquid surface at the ridge), the minimal value of L can be estimated using geometrical optics and is given by the approximate relationship [8]

$$L_{\min} \cong \{H + R[1 - \cos(\varphi_f)]\} \\ \times \tan \left\{ \sin^{-1} \left[n_L \times \sin \left(\alpha_f - \varphi_f - \frac{\alpha_f - \gamma}{n_L} \right) \right] + \varphi_f \right\} \\ + R \sin(\varphi_f), \quad (2)$$

where n_L is the refractive index of the liquid [9]. In practice, though, the black-and-white interface can easily be adjusted prior to image acquisition (while the drum is rotating) through, for example, the use of a translation stage upon which the CP is placed, in a manner that will allow for an optimal observation of surface perturbation dynamics.

As is evident from Fig. 2(c), the black-and-white contrast plane enables a clear visualization of surface perturbations, which would otherwise be undetectable (i.e., with a uniform background). However, in order to acquire *quantitative* measurements of free surface activity, one has to overcome two sources of bias intrinsic to OCT. The first is a translation bias, associated with the fact that perturbations farther away from the front (i.e., closer to the black-and-white interface) need not be as strong as ones closer to the interface in order to be detected by the method. The second has to do with the fact that the free surface is curved. Thus, light rays passing through regions having a relatively steep slope, such as near the front, will refract more strongly than regions farther from the front. Note that these sources of bias tend to cancel each other. In the following section, we present a way to overcome these sources of bias, which allows for quantitative measurements of surface perturbations.

C. Obtaining quantitative measurements of surface perturbations using OCT

Obtaining quantitative data pertaining to surface perturbations can be achieved by using a linear gray-scale transient region between the white-and-black parts of the contrast plane (Fig. 3). As we show below, this simple improvement enables a rigorous conversion of the image recorded by the CCD camera to an angular measurement of surface perturbations.

An important ingredient in the process of conversion from CCD intensity image to angular perturbations is the undisturbed 2D shape of the liquid surface, captured by the reflex camera positioned on the axis of rotation (see Fig. 1). Figure 4(a) depicts a typical image taken by the reflex camera. The image, taken for the case in which the drum is partially filled ($V^* = 0.1$) with an 80 ppm polymer solution and rotating at $\Omega = 0.09 \text{ s}^{-1}$, is processed using appropriate software in order to fit the liquid interface. This is done for every rotation

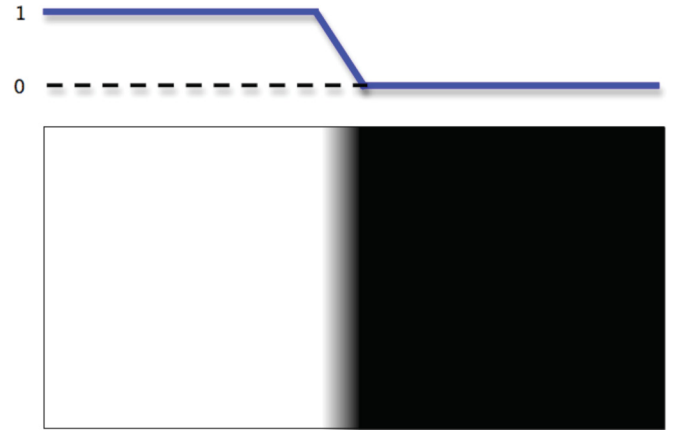


FIG. 3. (Color online) Contrast plane with a linear gray-scale transient region. The top part of the figure shows the variation of the intensity along the contrast plane.

rate examined, and yields the reference (or rest) shape of the liquid surface $\alpha_0(\mathbf{r}_0, \Omega)$ (see Fig. 4).

Within the region of interest of the CCD image, one now has rays which originate from the white part (normalized intensity $I = 1$), rays which originate from the black part ($I = 0$), and rays which originate at the gray-scale region ($0 < I < 1$). For the latter case, to leading order, the instantaneous angular perturbation to the rest shape at a point \mathbf{r}_0 on the surface is related to the intensity at the corresponding location through [6]

$$\Delta\alpha(\mathbf{r}_0, t) \equiv \alpha(\mathbf{r}_0, t) - \alpha_0(\mathbf{r}_0) \\ \cong [\alpha_2(\mathbf{r}_0) - \alpha_1(\mathbf{r}_0)] [1 - I(\mathbf{r}_0, t)] \\ + [\alpha_1(\mathbf{r}_0) - \alpha_0(\mathbf{r}_0)], \quad (3)$$

where the functions $\alpha_1(\mathbf{r}_0)$ and $\alpha_2(\mathbf{r}_0)$ are surface angles corresponding to rays emerging from the beginning and end of the gray region onto the CCD camera (i.e., at distances L_1 and L_2 from the vertical plane through the rotation axis), respectively [Fig. 4(b)]. These functions are attained from the rest shape $\alpha_0(\mathbf{r}_0)$ and the given values γ , n_L , H , L_1 , and L_2 , through the use of specifically designed, geometrical optics-based software. Figure 4(c) shows a typical example of the calculated critical angular difference $\alpha_1 - \alpha_0$, which is used in Eq. (3).

Thus, through the use of Eq. (3), we are able to obtain quantitative data concerning free-surface perturbations. In most practical cases, in which there is a need for quantitative data on surface perturbation, the detection of each localized perturbation in the raw intensity field given by I is done through a number of steps, depicted in Fig. 5. The raw CCD image is shown in Fig. 5(a) (the lower part of the image coincides with the liquid front line). This image is then flattened using a background image based on an average of a large number of images, and normalized. The negative of the resultant normalized image [i.e., $[1 - I(\mathbf{r}_0, t)]$; see Fig. 5(b)] is then substituted into Eq. (3) for conversion to an angular field. The active (perturbed) areas are then detected [gray regions in Fig. 5(c)]. One next uses an angular threshold (e.g., 0.35 rad) in order to determine the exact boundary of the sought-after perturbed areas [white boundary line in Fig. 5(c)].

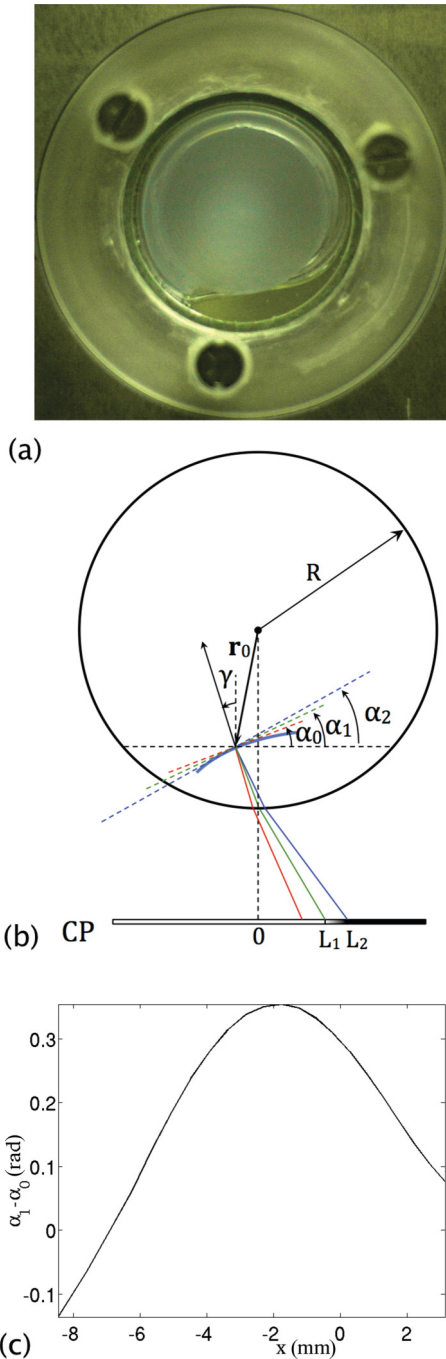


FIG. 4. (Color online) Extracting information from the side view of a liquid surface. (a) A typical “on-axis” raw image, taken for an 80 ppm polymer solution with $V^* = 0.1$ and $\Omega = 0.09 \text{ s}^{-1}$, from which the liquid surface [i.e., $\alpha_0(\mathbf{r}_0)$] is reconstructed using computational tools. (b) Schematic illustration of ray-tracking analysis, which allows one to extract the functions α_1 and α_2 used in Eq. (3) in order to get a quantitative measure of surface perturbations. The three rays depicted represent three scenarios corresponding to different slopes of the free surface at \mathbf{r}_0 . The red ray, which originates from the white part of CP, corresponds to the rest shape scenario ($\alpha = \alpha_0$). The green ray, which originates at the beginning of the gray region, corresponds to a steeper slope $\alpha = \alpha_1$. The blue ray, which originates at the end of the gray region, corresponds to an even steeper slope $\alpha = \alpha_2$. Note that in all cases, the rays are refracted toward the CCD camera. (c) Dependence of $(\alpha_1 - \alpha_0)$ on the horizontal coordinate.

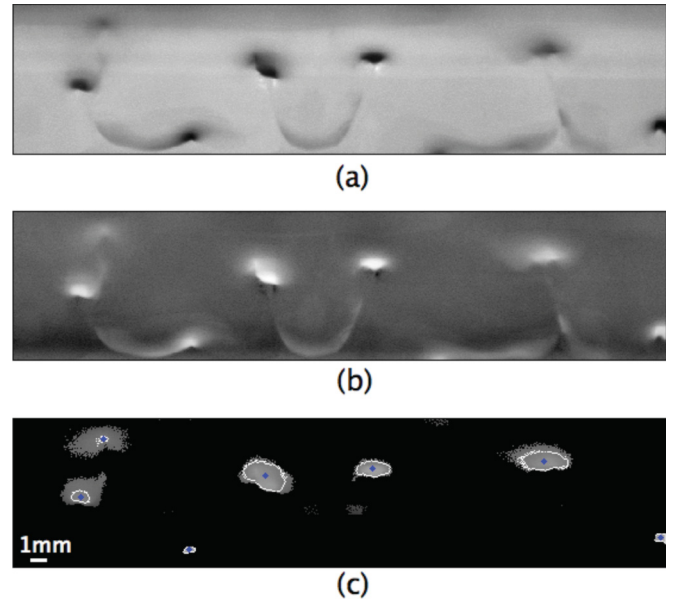


FIG. 5. (Color online) Stages in detection of surface perturbations. The raw CCD intensity image is depicted in (a). This image is then flattened using a background image and normalized. The negative of the resultant image (i.e., $[1 - I(\mathbf{r}_0, t)]$), which is substituted into Eq. (3), is depicted in (b). Detection of plume area is depicted in (c). At first one determines activity regions (gray area) and utilizes Eq. (3) to convert the intensity in these regions to angular perturbation measurements. A desired threshold (e.g., 0.35 rad) is then used to determine the boundaries of the corresponding localized perturbations (white border line). The lower part of the images coincides with the front line.

III. RESULTS

The experimental investigation presented in this section focuses on surface dynamics observed for dilute polymeric solutions (i.e., $c_p \leq 100 \text{ ppm}$) partially filling the rotating horizontal drum. These intriguing non-Newtonian liquids exhibit unique instabilities at low Reynolds numbers $\text{Re} = \Omega R d_p / \nu$ (here ν is the kinematic viscosity and $d_p = \sqrt{\nu \Omega R / g}$ is the characteristic depth of the liquid pool derived through comparing viscous and gravity forces), due to the relatively large Weissenberg numbers $\text{Wi} = \lambda \Omega R / d_p$. The latter conveys the predominance of the nonlinear elastic stresses over dissipation due to polymer relaxation. While there are several parameters which govern the dynamics of rimming flows of polymer solutions, we have focused on the effect of the rotation rate, the polymer concentration, and, to a lesser extent, the volume fraction.

A. Localized coherent structure (plume) dynamics

In rimming flow of a polymeric solutions the liquid front is unstable to an elastically driven instability at relatively low rotation rates and negligible Reynolds numbers. These instabilities result in localized coherent structures, also termed surface plumes. They originate at the front and move *upstream* on the surface of the recirculating liquid layer, where they eventually decay.

Figure 6(a) depicts different stages in the evolution of a typical surface plume, observed for a 40 ppm polymer solution.

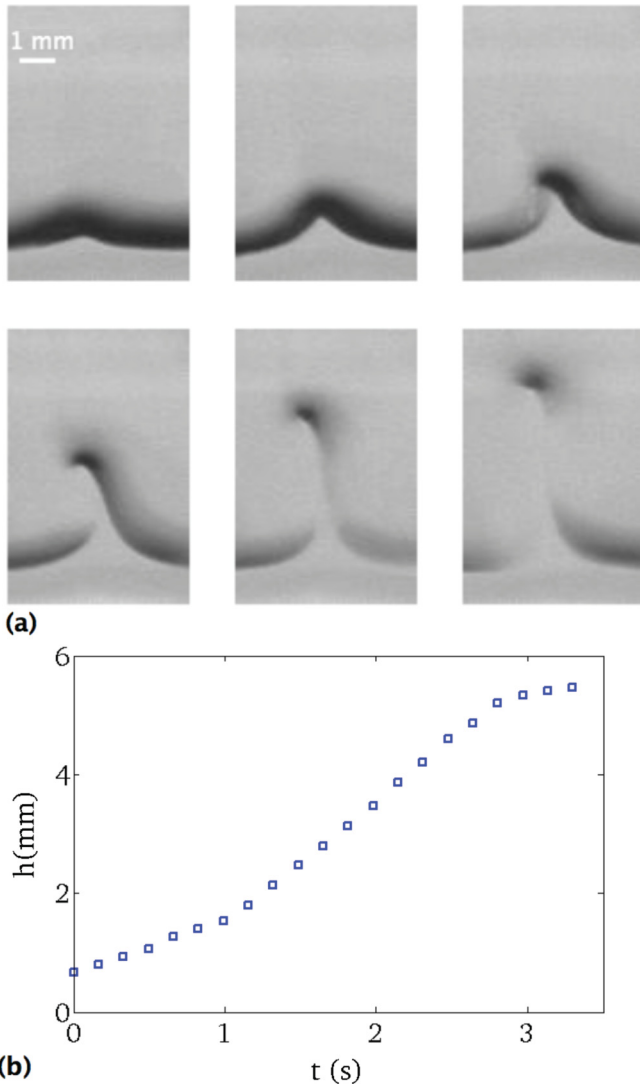


FIG. 6. (Color online) Evolution of a single plume. (a) Time series ($\Delta t = 0.6$ s) depicting evolution of a single plume, originating at the ridge. (b) Height of the plume (i.e., distance from the front, along the surface) as a function of time.

The filling fraction in this instance was $V^* = 0.1$ and the rotation rate $\Omega = 0.17$ s $^{-1}$. Figure 6(b) shows the height h (distance from the front, along the free surface) of the plume as a function of time. One can distinguish three main generic regions. The first region is characterized by an almost uniform velocity motion, and corresponds to the initial development and “pinch-off” of the plume from the front. The second region is characterized by a uniform velocity motion (which is larger than that found in the first stage) away from the front, while in the third region the plume reaches a saturation height and the velocity vanishes.

As the main control parameter (i.e., the rotation rate Ω) is increased from the onset of the elastic instability to the point where the liquid pool redistributes itself to form an almost uniform layer coating the inner cylinder wall, the surface plumes first grow in size and then saturate. This behavior is depicted in Fig. 7, where the mean plume height as a function of rotation rate is presented for the case $c_p = 20$ ppm.

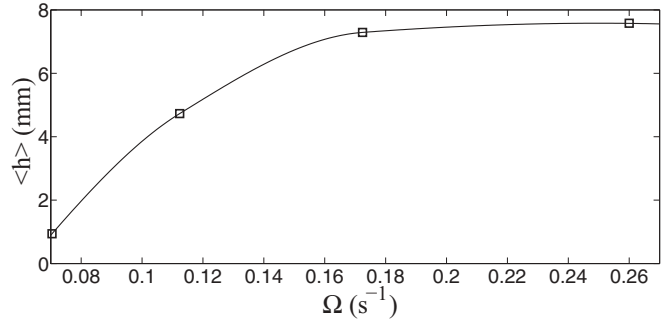


FIG. 7. Dependency of mean plume height on rotation rate for a 20 ppm polymer solution. The volume fraction is $V^* = 0.1$. The solid line is a guide to the eye.

B. Collective dynamics and coalescence of surface plumes

Depending on the filling fraction of the liquid, the rotation rate, and the elasticity of the polymeric solution (characterized by the relaxation time λ), different collective dynamics can be observed for surface perturbations. For relatively low volume fractions and large relaxation times (≈ 10 s), a dominant feature of surface plume dynamics is coalescence, whereby small plumes merge to form larger plumes. Figure 8(a) shows successive stages in the coagulation process of two plumes as they move away from the front. Figure 8(b) shows the corresponding distance as a function of time. As can be seen from the graph, at first the plumes move almost parallel to each other and then approach each other with an almost constant velocity prior to merging.

While the dynamics observed following the instability of the liquid front for relatively large relaxation times and low filling fractions is generally chaotic, for smaller polymeric relaxation times and larger values of filling fractions the dynamics observed is more steady and coherent. Figure 9 shows a typical image of equally spaced, long-lived solitary surface plumes. These periodic solitary plume structures can move either to the left or to the right. Furthermore, the interaction between adjacent plumes is such that they will coalesce if the distance between them is smaller than a critical value (equal to about 20 mm in the case depicted in Fig. 9).

C. Surface plume statistics

Exploring the statistics of surface plumes reveals additional information regarding the underlying physics. In particular, a quantitative measurement of the surface perturbation area s allows one to study important statistical aspects, such as the properties of the area distribution function $D(s)$ and the autocorrelation function $A(\tau) = \langle I(t), I(t + \tau) \rangle$.

We elaborated above (Sec. III B) on a predominant feature in the dynamics of surface plumes, namely their tendency to coagulate and form larger surface plumes for low volume fractions and large relaxation times. Coagulation is central to a wide range of physical, chemical, and biological processes, and an understanding of its kinetics and scaling is of considerable importance in many basic and applied problems, from aerosol and polymer science to cloud physics and cluster formation in galaxies.

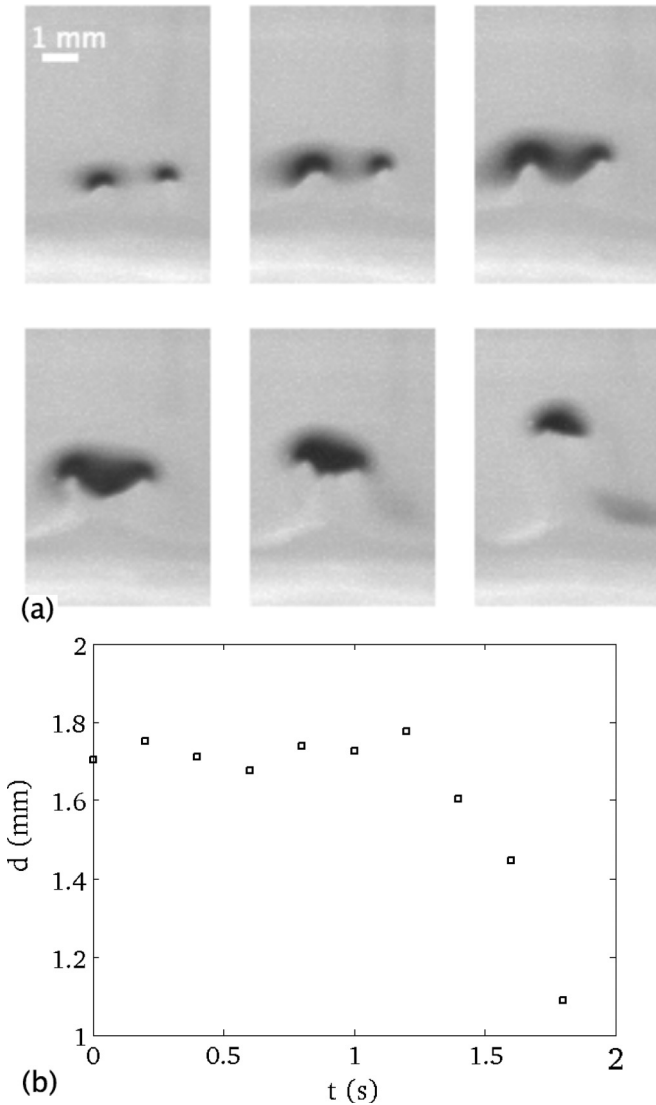


FIG. 8. Plume coagulation. (a) Successive stages in the coagulation of surface plumes for a 40 ppm polymer solution rotating at $\Omega = 0.12 \text{ s}^{-1}$. The time step between frames is 0.5 s. The filling fraction in this instance is $V^* = 0.1$. (b) Distance (center-to-center) between the merging plumes as a function of time.

Mean-field description of coagulation kinetics is modeled by the Smoluchowski equation [10]. The physical picture behind the model is that of droplets of different masses (sizes) moving randomly in space. When two droplets collide, they merge to form a new droplet whose mass is the sum of the constituent droplets. The coagulation is irreversible—large droplets do not break up into smaller droplets.

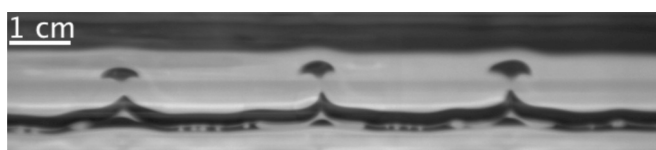


FIG. 9. Periodically spaced solitary plumes observed with OCT for a low relaxation time, 100 ppm polymer solution. The volume fraction in this instance is $V^* = 0.25$.

The Smoluchowski equation, written in symmetrical form and in the presence of a source and a sink, is [11]

$$\frac{\partial D(s,t)}{\partial t} = \frac{\sigma}{2} \int_0^\infty K(s_1,s_2)D(s_1,t)D(s_2,t) \times [\delta(s - s_1 - s_2) - \delta(s - s_1) - \delta(s - s_2)]ds_1ds_2 + \frac{J_0}{s_0}\delta(s - s_0) - \frac{J}{S}\delta(s - S), \quad (4)$$

where $D(s,t)$ is the instantaneous area (or mass) distribution function, $K(s_1,s_2)$ is the coagulation kernel, which conveys the affinity of two plumes to irreversibly merge, and σ is the coagulation rate coefficient. In the integral, the first Dirac δ function represents the gain in $D(s,t)$ due to coagulation of smaller droplets of sizes s_1 and s_2 , while the second and third account for losses due to merging. The two additional terms in Eq. (4) are source (at scale s_0) and sink (at scale S) terms.

In many cases, the coagulation process is time-dependent due to the fact that there is no mechanism that acts as a sink in the system. As a result, the system goes through a gelation transition [12]. From a mathematical point of view, the sink term in Eq. (4) is absent and the distribution function diverges at finite time. In contrast, the above equation permits stationary solutions of the form [11]

$$D(s) \sim (J_0/\sigma)^{1/2}s^{-(3+\zeta)/2}, \quad (5)$$

where ζ denotes the degree of homogeneity of the kernel.

Our system is a unique example in which both source (i.e., elastically driven plumes at small scales) and sink (decay of plumes at large scales) are present. This allows for the experimental investigation of a steady-state coagulation process through the measurement of the area distribution function. Figure 10 shows $D(s)$ corresponding to the dynamics observed for different values of rotation rate for an 80 ppm polymer solution. In general, one can distinguish between two different dependencies of $D(s)$. For low plume areas, the distribution decreases in a moderate way, while for relatively large areas the dependency is a power-law dependency. The

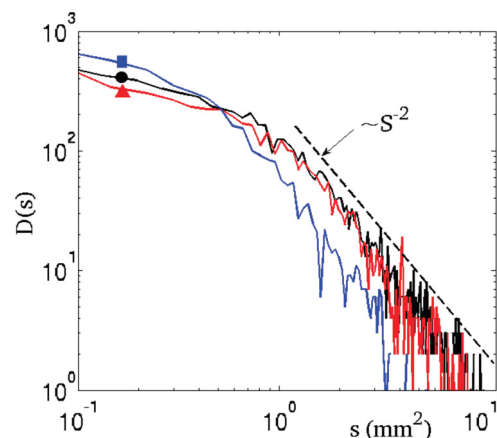


FIG. 10. (Color online) Plume area distribution function. The three cases depicted correspond to an 80 ppm polymer solution with $V^* = 0.1$ and $\Omega = 0.15 \text{ s}^{-1}$ (black circle), $\Omega = 0.13 \text{ s}^{-1}$ (red triangle), and $\Omega = 0.09 \text{ s}^{-1}$ (blue square). The dashed line depicts a power law with exponent -2 .

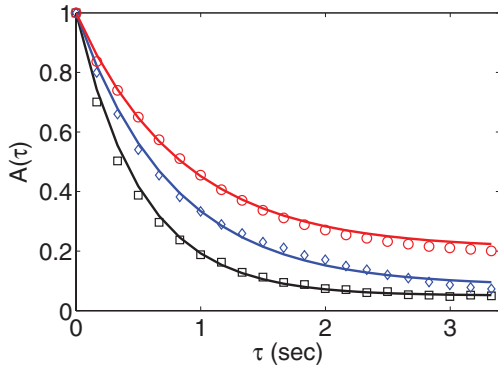


FIG. 11. (Color online) Autocorrelation function. The three cases depicted correspond to $c_p = 20$ ppm, $\Omega = 0.26$ s $^{-1}$ (black square); $c_p = 40$ ppm, $\Omega = 0.17$ s $^{-1}$ (red circles); and $c_p = 80$ ppm, $\Omega = 0.125$ s $^{-1}$ (blue diamonds). The corresponding characteristic decay times are $\tau_c = 0.48, 0.77,$ and 0.70 s. In all cases, $V^* = 0.1$.

dashed line shown for comparison in Fig. 10 has a (-2) exponent.

To employ Smoluchowski's mean-field approach, we utilize a widely used droplet coagulation model, first proposed by Saffman and Turner [13]: $K(s_1, s_2) = (s_1^{1/2} + s_2^{1/2})^2$. In this case, $\zeta = 1$ and thus the steady-state form of the area distribution function is $D(s) \sim s^{-2}$. This is in agreement with the experimental data for the large plume area regime, presented in Fig. 10.

Another important statistical result, obtained through the use of OCT, has to do with the chaotic characteristic of surface plume dynamics. Figure 11 presents the autocorrelation $A(\tau)$, which conveys the measure of temporal coherence pertaining to the dynamics of the surface plumes, for three different cases. The three graphs are characterized by a decay time which is considerably smaller than the characteristic time period Ω^{-1} , indicating a relatively fast loss of temporal coherence.

IV. DISCUSSION

In this work, we have described a detail experimental investigation into the emergence and evolution of elastically driven surface plumes observed in the rimming flow of a polymer solution. The phenomenon of surface plumes was investigated for different polymer concentrations and for a range of rotation rates. We studied single plume dynamics as well as the statistics pertaining to the collective dynamics of the plumes. Both dynamical aspects are strongly effected by plume coagulation. In particular, the area distribution function shows a power-law dependency which is consistent with the Smoluchowski model of plume coagulation. The chaotic characteristics of the phenomenon are manifested by

the fast loss of temporal coherence represented through the autocorrelation function.

A number of theoretical investigations on rimming flows of non-Newtonian fluids were reported in recent years. These mainly focused on the shape of the liquid front in the plane perpendicular to the axis of rotation [14]. A rigorous theoretical analysis of the phenomenon presented in the current work is, however, lacking. In particular, such an investigation should address the interaction of plumes, which leads to plume coagulation and the observed power-law dependency of $D(s)$. In this respect, it should be noted that due to the relatively large values of the Weissenberg number [$Wi = O(10)$] associated with the flow within the recirculating pool, the phenomenon is intrinsically nonlinear.

We elaborated on the optical contrast technique (OCT) used in our experiments, which is a powerful tool through which previously unexplored surface dynamics can now be studied in detail. The technique can be used in order to either visualize the active regions of the free liquid surface or obtain quantitative measurements of the corresponding perturbations with respect to the rest shape of the surface. It is important to note that the applicability of OCT is not restricted to non-Newtonian liquids and can be used in the same manner for the investigation of surface dynamics in Newtonian liquids. Moreover, the scope of applications might be extended from the geometry of the rotating drum to other free liquid surface phenomena providing that the spatial extent of the dynamics is not too large in the direction perpendicular to the black-and-white interface (or gray transient region) of the contrast plane. One example is coating flow over an inclined plane. Another example is free surface perturbations in shallow pools. Here one would prefer an annulus geometry for the contrast plane (i.e., an inner white circle surrounded by a gray-scale ring with a surrounding black region) with the CCD camera positioned at right angle to the liquid surface ($\gamma = 0$).

Similar to other experimental techniques, OCT has limitations. In the current implementation of OCT, where a 1D straight line (or gray-scale strip) separates the black-and-white parts of the plane, the CCD camera detects surface perturbations through collecting rays from an angle up to 180° . This means that the front (or upper) part of the localized plume is detected while its rear (or lower) part is not. In particular, this would mean that the detected area of the plume is half the actual perturbed area if one assumes an elliptic plume head. This limitation can be overcome if one uses a contrast plane with a different geometry, such as the annulus discussed above for implementation in free surface perturbations of shallow pools. However, as a result of using a closed boundary between the two parts of the contrast plane, one restricts oneself to the study of local regions.

- [1] G. Seiden and P. J. Thomas, *Rev. Mod. Phys.* **83**, 1323 (2011).
 [2] F. Melo and S. Douady, *Phys. Rev. Lett.* **71**, 3283 (1993).
 [3] S. T. Thoroddsen and L. Mahadevan, *Exp. Fluids* **23**, 1 (1997).
 [4] D. P. Vallette, W. S. Edwards, and J. P. Gollub, *Phys. Rev. E* **49**, R4783 (1994).

- [5] R. T. Balmer, *Nature (London)* **227**, 600 (1970).
 [6] G. Seiden and V. Steinberg, *Europhys. Lett.* **96**, 28004 (2011).
 [7] Y. Liu, Y. Jun, and V. Steinberg, *J. Rheol.* **53**, 1069 (2010).

- [8] For smaller values of L , the close vicinity of the front will appear black even with no perturbations present. As a result, it will not be possible to extract quantitative information regarding surface perturbations from these locations.
- [9] Here we assume a negligible effect due to the cylinder wall.
- [10] M. von Smoluchowski, *Z. Phys. Chem.* **92**, 129 (1917).
- [11] C. Connaughton, R. Rajesh, and O. Zaboronski, *Phys. Rev. E* **69**, 061114 (2004).
- [12] A. Lushnikov, *Isv. Akad. Nauk SSSR, Ser. Fiz. Atmosfer. I Okeana* **14**, 738 (1978).
- [13] P. G. Saffman and J. S. Turner, *J. Fluid Mech.* **1**, 16 (1956).
- [14] S. Fomin, T. Hashida, and J. Watterson, *J. Non-Newtonian Fluid Mech.* **111**, 19 (2003); S. Fomin, *J. Fluids Eng.* **128**, 107 (2006); J. Sanders, D. D. Joseph, and G. S. Beavers, *J. Non-Newtonian Fluid Mech.* **9**, 269 (1981).